Time-Resolved X-Ray Imaging of Anisotropic Nanoplasma Expansion

Christian Peltz,[1,*] Charles Varin,[2] Thomas Brabec,[2] and Thomas Fennel[1,†]
[1]*Institut für Physik, Universität Rostock, 18051 Rostock, Germany*
[2]*Department of Physics, University of Ottawa, 150 Louis Pasteur, Ontario K1N 6N5, Canada*
(Received 27 November 2013; published 23 September 2014)

A complete time-resolved x-ray imaging experiment of laser heated solid-density hydrogen clusters is modeled by microscopic particle-in-cell simulations that account self-consistently for the microscopic cluster dynamics and electromagnetic wave evolution. A technique is developed to retrieve the anisotropic nanoplasma expansion from the elastic and inelastic x-ray scattering data. Our method takes advantage of the self-similar evolution of the nanoplasma density and enables us to make movies of ultrafast nanoplasma dynamics from pump-probe x-ray imaging experiments.

DOI: 10.1103/PhysRevLett.113.133401 PACS numbers: 36.40.-c, 42.25.Fx, 42.30.Wb, 52.50.Jm

The unique pulse characteristics of x-ray free-electron lasers (XFELs) [1,2] promise striking new applications. The high photon flux permits single-shot structural analysis of nanomaterials [3] and biomolecules [4] via x-ray diffraction. In combination with the few femtosecond XFEL pulse duration, this allows time- and space-resolved diffractive imaging of single objects, with the ultimate goal of visualizing ultrafast dynamics in matter with atomic-scale resolution [5,6].

In this Letter, we theoretically study the feasibility of near-infrared (NIR) pump XFEL probe imaging of nanoplasma dynamics. Exposure to intense NIR fields turns solid-density materials into localized, highly ionized finite plasmas that expand on a femtosecond time scale. This dynamics is important for a wide range of processes, such as subwavelength laser machining [7]; the generation of ultrashort x-ray, electron, and ion pulses from surfaces [8,9], foils [10–15], clusters [16,17], or droplets [18,19]; and laser Coulomb explosion imaging of molecules [20]. So far, experimental access to the femtosecond nanoplasma dynamics is challenging and has been mostly indirect, e.g., via the analysis of final spectra of electrons, ions, and emitted radiation. This limits insight into the underlying physics and impedes understanding and optimization of the above processes.

Dynamic XFEL imaging presents a promising route towards a direct visualization of ultrafast dynamics in finite solid-density plasmas with nanometer resolution, which would substantially extend the capability of existing real-time plasma imaging techniques [10,21–25]. Its experimental feasibility has been demonstrated in recent proof-of-principle investigations of clusters; cluster size [26] and shape [27] have been measured in static experiments, and signatures of transient phenomena have been observed [28]. However, to enable dynamical imaging in practice, a method for inversion and interpretation of the scattering data is needed. This remains challenging for various reasons: First, the phase of the scattered field is missing; second, transient changes complicate retrieval; and third, probing with high x-ray intensity may introduce additional dynamics [29]. Here we explore a first idea on how to retrieve the NIR induced electron density evolution quantitatively from the x-ray scattering intensity.

In order to develop and test retrieval methods, complete knowledge of both the NIR pump dynamics and the XFEL probe process is needed. This requires a self-consistent first-principle description of plasma dynamics and electromagnetic field evolution, including elastic and inelastic classical x-ray scattering. The particle dynamics may be described classically, as intense laser pulses turn the target quickly into a nondegenerate plasma. However, many-particle correlations and plasma microfields need to be resolved, as (i) NIR laser driven solid-density plasma dynamics mostly takes place in the regime of strongly coupled plasmas [30], and (ii) short x-ray wavelengths probe atomic-scale plasma fluctuations. Conventional techniques, such as molecular dynamics and (collisional) electromagnetic particle-in-cell codes, miss either wave propagation or the atomic-scale plasma correlations and fluctuations. Therefore, they cannot deliver a complete account of the pump-probe process. The above requirements are met by the microscopic particle-in-cell (MicPIC) technique [31] used in our analysis.

For clarity, our numerical MicPIC imaging experiment focuses on the simplest nanoplasma representative, a solid-density hydrogen cluster, and reveals the following:

(i) We find an anisotropic self-similar electron density expansion that can be represented by an analytical profile. The evolution can be captured by two time- and direction-dependent parameters (core radius, surface width). The core electron density remains constant.

(ii) A clear correspondence is established between density profile parameters and features in the scattering data; core radius and surface layer width determine fringe spacing and angular decay of the elastically scattered x-ray intensity; the core electron density determines the shift of the inelastic plasmon peak.

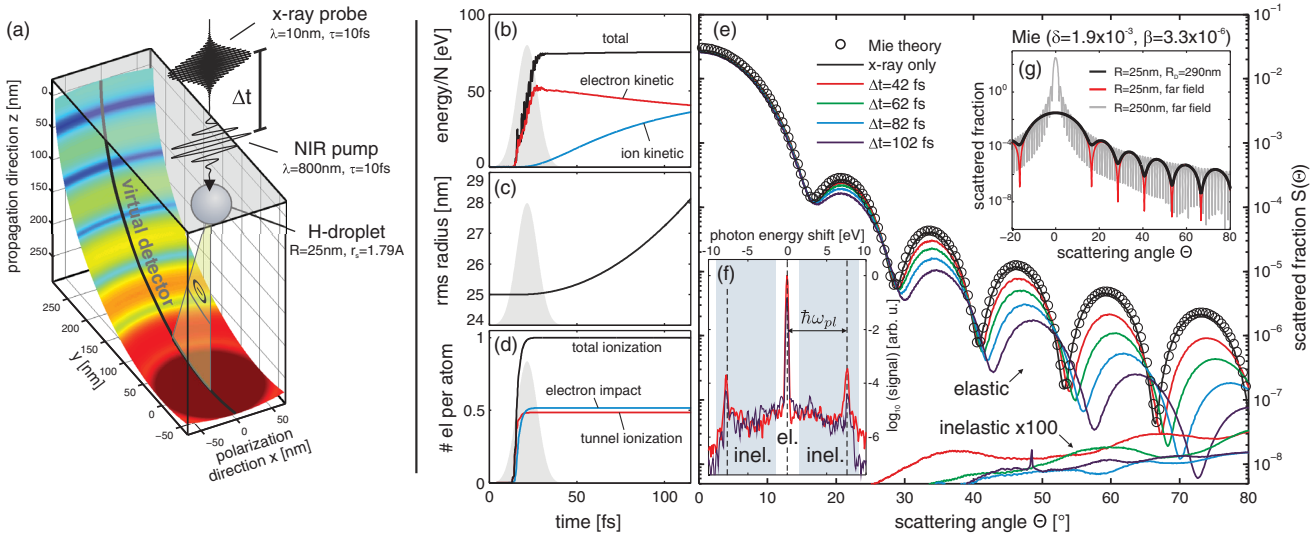

FIG. 1 (color). (a) Sketch of the simulation setup with the $R = 25$ nm hydrogen cluster, the virtual detector (defined by a sphere with radius $R_d = 290$ nm around the cluster center), and the incident laser fields. (b)–(d) Time evolution of selected observables during and after the NIR pump excitation. (e) Resulting elastic and inelastic scattered fraction (detection in the y-z plane) for different x-ray probe delays and the Mie-theory result for an unexpanded cluster for comparison. In the limit $R_d \to \infty$, $S(\Theta)$ specifies the number of x-ray photons scattered into an element of solid angle per incident photon impinging on the initial geometric cluster cross section. (f) Scattered x-ray intensity spectrum (averaged over $60° < \Theta < 90°$) with elastic and inelastic contributions. (g) Mie results showing the minor impact of the finite MicPIC detector distance (black vs red lines) and the size-independent universal envelope of the elastically scattered fraction for weakly absorbing spheres (gray line).

(iii) Based on the self-similar plasma profile parametrization, a retrieval method for dynamic x-ray imaging is developed that will enable XFELs to make movies of laser induced expansion dynamics of finite nanoplasmas. The method is demonstrated for clusters; potential applications to other finite plasma systems with self-similar expansion, such as nanodroplets, thin foils, or nanorods, will be discussed at the end.

For our analysis, we consider spherical $R = 25$ nm solid-density hydrogen clusters (2.7×10^6 atoms, fcc structure, atomic Wigner-Seitz radius $r_s = 1.79$ Å). Tunnel and electron impact ionization of the atoms are modeled by effective quantum rates [32]. Resulting ions and plasma electrons are modeled by Gaussian charge distributions $\rho(r,w) = q\exp(-r^2/w^2)/\pi^{3/2}w^3$ with particle charge q and width parameter $w = 0.85$ Å, such that the classical electron-proton binding energy fits the atomic hydrogen ground state energy of $E_0 = -13.6$ eV. On the PIC level, particles are treated as Gaussian distributions with a larger width of $w_{\mathrm{pic}} = 1.14\Delta x$; this automatically specifies the range over which charged particle interactions have to be corrected on the Mic level [31]. Electric and magnetic fields on the PIC level are propagated by solving Maxwell's equations on a staggered, equidistant spatial grid with resolution $\Delta x = 4$ Å, ensuring proper sampling of the x-ray field. Both the NIR pump (800 nm, 10^{15} W/cm^2) and x-ray probe (10 nm, 10^{16} W/cm^2) pulses are plane waves with a 10 fs Gaussian temporal intensity envelope (FHWM), are polarized in x direction, and propagate in z direction [see Fig. 1(a)]. A full run takes about 30 days on an 80 core (8 × Intel E7-8860) shared memory workstation.

The NIR pump pulse induces rapid plasma formation; tunnel and impact ionization deplete the hydrogen atoms and create a fully inner ionized cluster near the pulse peak [Fig. 1(d)]. Cluster expansion starts immediately due to the low proton mass [Fig. 1(c)]; the electron kinetic energy decrease indicates hydrodynamic expansion [Fig. 1(b)]; additional ion acceleration via Coulomb explosion is evident from the fact that the ion kinetic energy gain is stronger than the decrease in electron kinetic energy. Eventually, about 80 eV per atom is absorbed.

The cluster dynamics is imaged by soft x-ray probe pulses for various pulse delays; see Fig. 1(e). Our calculations show that inverse bremsstrahlung heating due to the x-ray pulse is negligible, such that the NIR induced nanoplasma dynamics in Figs. 1(b)–1(d) is not distorted. For each delay, the time-dependent, angular-resolved scattered electric fields are recorded on a virtual detector [Fig. 1(a)] and frequency filtered to isolate and extract the elastic and inelastic x-ray scattering signal [Fig. 1(f)]. From the respective scattered transverse electric fields $E_\perp^{\mathrm{el/inel}}(\Theta, t)$, we calculate the scattered fractions

$$S^{\mathrm{el/inel}}(\Theta) = \frac{\varepsilon_0 c R_d^2}{\pi R^2 F_0} \int [E_\perp^{\mathrm{el/inel}}(\Theta, t)]^2 dt, \qquad (1)$$

with ε_0 the vacuum permittivity, c the speed of light, R_d the detector distance, and $F_0 \approx I_0\tau$ the fluence of the incident

x-ray field. An x-ray–only run with electrons placed at rest on top of the ions was used to validate the elastic MicPIC data against Mie calculations [Fig. 1(e)].

The MicPIC pump-probe scattering spectra [Fig. 1(f)] are dominated by the elastic contribution. The inelastic signal with two symmetric satellite peaks is due to coupling with longitudinal plasmon excitations. The plasmon exists as part of the thermal electron density fluctuations and leads to Raman-type scattering; the collective motion imprints an additional modulation on the scattered field that creates the satellites. Whereas the pronounced interference fringes of the elastic signal decay with increasing angle, the inelastic signal increases with angle, does not exhibit interference fringes, and fluctuates with delay; see Fig. 1(e). The spectral plasmon satellites are a key diagnostic tool in plasma x-ray Thomson scattering [33,34] and provide a sensitive measure of the plasma electron density. In the MicPIC data, the spectral shift of the peaks is independent of delay [cf. Fig. 1(f)] and matches the volume plasmon energy $\hbar\omega_{\mathrm{pl}} = 7.6$ eV for fully ionized hydrogen at the initial cluster density.

The elastic MicPIC scattering images [Fig. 1(e)] reveal two main pump-probe delay effects. (i) The slope of the elastic scattering signal increases with delay, resulting in a signal drop by more than one order of magnitude. (ii) The fringe separation increases continuously with pulse delay. Assuming a sphere, this trend would correspond to a reduction of cluster size, which seems to be in striking contradiction to the increasing radius in Fig. 1(b). To resolve this apparent contradiction, a more detailed analysis of the expansion dynamics is needed.

Figure 2 shows direction-resolved radial density profiles of electrons and ions averaged over cones ($\pi/4$ full opening angle, cone apex at cluster center) aligned parallel (green) and perpendicular (blue) to the laser polarization. The density profile snapshots show that in early stages surface ions are unscreened and undergo rapid Coulomb explosion. The anisotropy of the ion spectra arises from the oscillating electron cloud (during NIR pump excitation) which periodically exposes the cluster poles; the effectively reduced charge screening at the poles results in stronger ion acceleration along the polarization axis [35–37]. After Coulomb expulsion of the surface ions, the remaining ion and electron densities overlap and screen each other, and the cluster continues to expand hydrodynamically.

In the hydrodynamic cluster expansion, the density profiles follow a self-similar shape, similar to the expansion predicted for a semi-infinite plasma [38,39]. The radial MicPIC electron density can be accurately described in all expansion stages by a sharpened Fermi distribution

$$n_e(r) = \frac{n_{\mathbf{c}}}{[\exp(\frac{r-r_{\mathbf{c}}}{ds}) + 1]^s}, \qquad (2)$$

with core density $n_{\mathbf{c}}$, core radius $r_{\mathbf{c}}$, and decay length d as a measure of the surface width; the sharpness factor s ensures the correct transition behavior between the two asymptotic

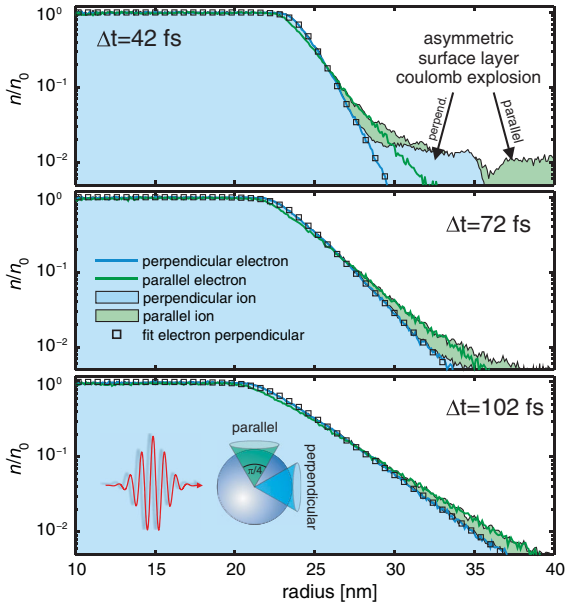

FIG. 2 (color). Radial electron and ion density profiles for different pulse delays (as indicated). Solid lines (electron) and shaded areas (ion) show density profiles extracted directly from the MicPIC simulation for directions parallel to (green) and perpendicular to (blue) the polarization direction. Open squares correspond to electron density fits perpendicular to the NIR polarization using the profile given in Eq. (2).

limits (Fig. 2). The parameter evolution is extracted by fitting Eq. (2) to the time-dependent MicPIC electron density [solid lines in Figs. 3(a)–3(c)]. The main features are linear decrease of the core radius $r_{\mathbf{c}}$ and linear growth of surface width d; the actual parameter values differ for parallel (green) and perpendicular (blue) profiles, reflecting the anisotropic expansion; the sharpness s converges rapidly and is thus of little relevance to the dynamics. As a result, the complex plasma expansion dynamics can be captured by two parameters, core radius and surface width.

Equipped with this knowledge, we can now explain the features, observed in the scattering images in Fig. 1(e), in terms of the density profile parameters. For the sake of simplicity, we first consider a spherical electron distribution with the radial density described by Eq. (2). In the first Born approximation and including polarization effects, the resulting scattering image is determined by

$$\mathbf{E}(\mathbf{r}_d) = \int_V \frac{\tilde{\mathbf{r}} \times (\mathbf{E}_0 \times \tilde{\mathbf{r}}) r_e e^{i(\mathbf{kr}+k\tilde{r})}}{\tilde{r}^3} n_e(r) d^3 r, \qquad (3)$$

where $\mathbf{k}$ is the incident x-ray wave vector, r_e is the classical electron radius, and n_e is taken from Eq. (2). Further, $\mathbf{E}_0$ and $\mathbf{E}$ are complex amplitudes of the incident field and the scattered field at detector position $\mathbf{r}_d$. The detector position in the frame of each scattering subvolume is denoted by $\tilde{\mathbf{r}} = \mathbf{r}_d - \mathbf{r}$. The scattered fraction in Born approximation is determined by $S_B(\Theta) = R_d{}^2 \hat{E}_\perp^2 / \pi R^2 \hat{E}_0^2$ and is analyzed in

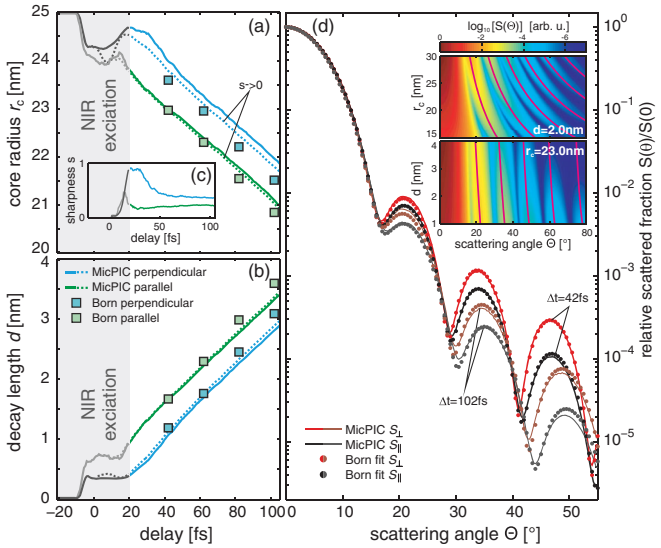

FIG. 3 (color). (a)–(c) Time evolution of density profile parameters; lines correspond to direct fits of the MicPIC density for directions parallel to (green) and perpendicular to (blue) the polarization direction using all parameters (solid) or the sharp edge limit $s \to 0$ (dashed); squares denote parameters reconstructed from the scattering pattern in the sharp edge limit (see text). (d) Full NIR–polarization dependent MicPIC scattering pattern (solid lines) and corresponding Born fits (circles) for two delays (as indicated); the inset shows a selective parameter analysis of the Born method for $s \to 0$ (see text).

the inset of Fig. 3 as a function of d and r_c in the limit $s \to 0$ (sharp edge). We find that the core radius r_c affects only the fringe separation without changing the envelope of the scattering signal. Vice versa, the decay length d mainly changes the slope of the envelope and modifies fringe positions only marginally. Consequently, the growing fringe spacing and signal drop for increasing delay in Fig. 1(e) can be explained by the shrinking core radius and cluster surface expansion.

Finally, we show that the self-similar density profile is key to reconstructing the anisotropic nanoplasma evolution from experimentally measured angular-resolved scattering images. To this end, Born scattering patterns are calculated from the analytical density profile $n(r,\theta)$ in Eq. (2) in the sharp edge limit ($s \to 0$) using anisotropic values for both core radius $r_c(\theta)$ and decay length $d(\theta)$; here θ is the angle with respect to the NIR polarization. For both parameters, we chose an angular dependence $\alpha(\theta) = \alpha_{\mathrm{perp}} + (\alpha_{\mathrm{par}} - \alpha_{\mathrm{perp}})\cos^2\theta$ to model an ellipsoidal density, resulting in a total of four free parameters. The sharpness is neglected, as it is irrelevant for the dynamics. The scattered fields are determined by inserting $n(r,\theta)$ into the Born expression Eq. (3). Optimal values of the four parameters are determined by simultaneously fitting Born images in the $x = 0$ ($S_\perp$) and $y = 0$ ($S_\parallel$) planes to corresponding MicPIC results via simplex optimization. We performed additional MicPIC runs with a rotated virtual detector to obtain the simulated $S_\parallel$ scattering data; the two directions mimic the full two-dimensional scattering images available in experiments. The examples in Fig. 3(d) illustrate that the anisotropic Born fits accurately describe the direction-resolved MicPIC scattering data.

The parameters retrieved from the MicPIC scattering images [squares in Figs. 3(a) and 3(b)] agree well with the parameters extracted directly from the MicPIC electron density profile. The anisotropic core radius and surface width evolution can be retrieved quantitatively; remaining small deviations reflect the idealization via the four-parameter geometry model. This proves the feasibility of our reconstruction method, which—together with experimental data—will enable direct dynamic imaging of electron density profiles. Since during the hydrodynamic expansion phase electron and ion profiles evolve together, the reconstructed profiles apply to both. Combining the elastic and inelastic scattering enables a fully quantitative reconstruction. The last missing parameter is the core electron density, which can be extracted from the plasmon peak in the scattering spectrum. Because of the weaker inelastic scattering, signal accumulation over many shots or higher x-ray intensities might be required for resolving the plasmon peaks.

Although our analysis has been restricted to hydrogen clusters, we expect qualitatively similar results for heavier element clusters with incomplete inner ionization. In these clusters, both bound and free electrons contribute to the elastic scattering image, and the x-ray probe pulse will generate additional plasma electrons via photo- and secondary ionization throughout the cluster. This will change the elastic scattering quantitatively through the difference in scattering factors of bound and free electrons; however, it will only weakly influence the relative signatures of the scattering image that are determined by the plasma geometry. Further, inelastic scattering depends on the free-electron density and is sensitive to x-ray induced ionization. The x-ray intensity dependent shift of the plasmon satellites presents a valuable diagnostic tool to measure the influence of x-ray probe pulses. Finally, the dynamics analyzed here in hydrogen clusters on a 100 fs time scale will take place on a longer time scale in heavier element clusters. We thus expect that the anisotropic plasma expansion dynamics can be resolved with the ~50 fs temporal resolution [40] currently available at free-electron laser facilities.

In conclusion, we reported a complete numerical experiment of dynamical x-ray imaging of clusters. The near-infrared induced anisotropic nanoplasma evolution can be efficiently described by a simplified ellipsoidal geometry model; the relevant model parameters, and therewith the complete electron density dynamics, can be quantitatively retrieved from x-ray scattering data. This, together with experiments in progress [41], opens a path towards making movies of finite plasma dynamics. Our method could be applied directly or with minor modifications to the study of little understood processes in clusters, such as anomalous

explosion [42], quasimonoenergetic ion generation via shock waves [43], distorted ion expansion through propagation-induced near fields [18], and ultrafast plasma wave dynamics [31]. Assuming self-similar spreading similar to the ellipsoidal cluster expansion, the generalization to more complex geometries like nanotubes or nanowires appears feasible, promising insight into the ultrafast high-density plasma formation at laser driven nanostructured metal surfaces [44]. Further potential applications are related to XFEL imaging of localized nanoplasmas at surfaces, e.g., for understanding the pulse structure dependence of subwavelength laser material machining in dielectrics [7] or for identifying optimal routes for localized laser modification of biological tissue [45]. In general, dynamic XFEL imaging of laser driven finite nanoplasmas will allow direct visualization and thereby a deeper understanding of fundamental ultrafast plasma processes relevant for a wide range of applications.

Financial support from the Deutsche Forschungsgemeinschaft within SFB 652/3 and SPP1391, as well as computer time provided by the North-German Supercomputing Alliance (HLRN) within Project No. mvp00004 and Calcul Québec/Compute Canada, are gratefully acknowledged.

*christian.peltz@uni-rostock.de
†thomas.fennel@uni-rostock.de

[1] K. Tiedtke, A. Azima, N. von Bargen, L. Bittner, S. Bonfigt, S. Duesterer, B. Faatz, U. Fruehling, M. Gensch, C. Gerth *et al.*, New J. Phys. **11**, 023029 (2009).
[2] P. Emma, R. Akre, J. Arthur, R. Bionta, C. Bostedt, J. Bozek, A. Brachmann, P. Bucksbaum, R. Coffee, F.-J. Decker *et al.*, Nat. Photonics **4**, 641 (2010).
[3] N. D. Loh, C. Y. Hampton, A. V. Martin, D. Starodub, R. G. Sierra, A. Barty, A. Aquila, J. Schulz, L. Lomb, J. Steinbrener *et al.*, Nature (London) **486**, 513 (2012).
[4] H. N. Chapman, P. Fromme, A. Barty, T. A. White, R. A. Kirian, A. Aquila, M. S. Hunter, J. Schulz, D. P. DePonte, U. Weierstall *et al.*, Nature (London) **470**, 73 (2011).
[5] H. N. Chapman, S. P. Hau-Riege, M. J. Bogan, S. Bajt, A. Barty, S. Boutet, S. Marchesini, M. Frank, B. W. Woods, W. H. Benner *et al.*, Nature (London) **448**, 676 (2007).
[6] A. Barty, J. Phys. B **43**, 194014 (2010).
[7] L. Englert, M. Wollenhaupt, L. Haag, C. Sarpe-Tudoran, B. Rethfeld, and T. Baumert, Appl. Phys. A **92**, 749 (2008).
[8] M. M. Murnane, H. C. Kapteyn, M. D. Rosen, and R. W. Falcone, Science **251**, 531 (1991).
[9] S. E. Irvine, A. Dechant, and A. Y. Elezzabi, Phys. Rev. Lett. **93**, 184801 (2004).
[10] L. Romagnani, J. Fuchs, M. Borghesi, P. Antici, P. Audebert, F. Ceccherini, T. Cowan, T. Grismayer, S. Kar, A. Macchi *et al.*, Phys. Rev. Lett. **95**, 195001 (2005).
[11] H. Schwoerer, S. Pfotenhauer, O. Jackel, K. Amthor, B. Liesfeld, W. Ziegler, R. Sauerbrey, K. Ledingham, and T. Esirkepov, Nature (London) **439**, 445 (2006).
[12] J. Fuchs, P. Antici, E. D'Humiéres, E. Lefebvre, M. Borghesi, E. Brambrink, C. Cecchetti, M. Kaluza, V. Malka, M. Manclossi *et al.*, Nat. Phys. **2**, 48 (2006).
[13] S. Steinke, A. Henig, M. Schnuerer, T. Sokollik, P. V. Nickles, D. Jung, D. Kiefer, R. Hoerlein, J. Schreiber, T. Tajima *et al.*, Laser Part. Beams **28**, 215 (2010).
[14] H. Daido, M. Nishiuchi, and A. S. Pirozhkov, Rep. Prog. Phys. **75**, 056401 (2012).
[15] A. Macchi, M. Borghesi, and M. Passoni, Rev. Mod. Phys. **85**, 751 (2013).
[16] U. Saalmann, C. Siedschlag, and J. M. Rost, J. Phys. B **39**, R39 (2006).
[17] T. Fennel, K.-H. Meiwes-Broer, J. Tiggesbäumker, P.-G. Reinhard, P. M. Dinh, and E. Suraud, Rev. Mod. Phys. **82**, 1793 (2010).
[18] T. V. Liseykina, S. Pirner, and D. Bauer, Phys. Rev. Lett. **104**, 095002 (2010).
[19] H. G. Kurz, D. S. Steingrube, D. Ristau, M. Lein, U. Morgner, and M. Kovacev, Phys. Rev. A **87**, 063811 (2013).
[20] M. Pitzer, M. Kunitski, A. S. Johnson, T. Jahnke, H. Sann, F. Sturm, L. P. H. Schmidt, H. Schmidt-Boecking, R. Doerner, J. Stohner *et al.*, Science **341**, 1096 (2013).
[21] N. H. Matlis, S. Reed, S. S. Bulanov, V. Chvykov, G. Kalintchenko, T. Matsuoka, P. Rousseau, V. Yanovsky, A. Maksimchuk, S. Kalmykov *et al.*, Nat. Phys. **2**, 749 (2006).
[22] P. Antici, J. Fuchs, M. Borghesiand, L. Gremilletand, T. Grismayerand, Y. Sentokuand, E. d'Humieresand, C. A. Cecchettiand, A. Mancicand, A. C. Pipahl *et al.*, Phys. Rev. Lett. **101**, 105004 (2008).
[23] S. Mondal, A. D. Lad, S. Ahmed, V. Narayanan, J. Pasley, P. P. Rajeev, A. P. L. Robinson, and G. R. Kumar, Phys. Rev. Lett. **105**, 105002 (2010).
[24] A. Buck, M. Nicolai, K. Schmid, C. M. S. Sears, A. Savert, J. M. Mikhailova, F. Kraus, M. C. Kaluza, and L. Veisz, Nat. Phys. **7**, 543 (2011).
[25] A. Borot, A. Malvache, X. W. Chen, A. Jullien, J. P. Geindre, P. Audebert, G. Mourou, F. Quere, and R. Lopez-Martens, Nat. Phys. **8**, 416 (2012).
[26] T. Gorkhover, M. Adolph, D. Rupp, S. Schorb, S. W. Epp, B. Erk, L. Foucar, R. Hartmann, N. Kimmel, K.-U. Kuehnel *et al.*, Phys. Rev. Lett. **108**, 245005 (2012).
[27] D. Rupp, M. Adolph, T. Gorkhover, S. Schorb, D. Wolter, R. Hartmann, N. Kimmel, C. Reich, T. Feigl, A. R. B. de Castro *et al.*, New J. Phys. **14**, 055016 (2012).
[28] C. Bostedt, E. Eremina, D. Rupp, M. Adolph, H. Thomas, M. Hoener, A. R. B. de Castro, J. Tiggesbaeumker, K.-H. Meiwes-Broer, T. Laarmann *et al.*, Phys. Rev. Lett. **108**, 093401 (2012).
[29] R. Neutze, R. Wouts, D. van der Spoel, E. Weckert, and J. Hajdu, Nature (London) **406**, 752 (2000).
[30] C. Peltz, C. Varin, T. Brabec, and T. Fennel, New J. Phys. **14**, 065011 (2012).
[31] C. Varin, C. Peltz, T. Brabec, and T. Fennel, Phys. Rev. Lett. **108**, 175007 (2012).
[32] T. Fennel, L. Ramunno, and T. Brabec, Phys. Rev. Lett. **99**, 233401 (2007).
[33] S. H. Glenzer, O. L. Landen, P. Neumayer, R. W. Lee, K. Widmann, S. W. Pollaine, R. J. Wallace, G. Gregori, A. Hoell, T. Bornath *et al.*, Phys. Rev. Lett. **98**, 065002 (2007).

[34] S. H. Glenzer and R. Redmer, Rev. Mod. Phys. **81**, 1625 (2009).
[35] V. Kumarappan, M. Krishnamurthy, and D. Mathur, Phys. Rev. A **66**, 033203 (2002).
[36] T. Fennel, G. Bertsch, and K.-H. Meiwes-Broer, Eur. Phys. J. D **29**, 367 (2004).
[37] B. N. Breizman, A. V. Arefiev, and M. V. Fomyts'kyi, Phys. Plasmas **12**, 056706 (2005).
[38] P. Mora, Phys. Rev. Lett. **90**, 185002 (2003).
[39] A. V. Gurevich, L. V. Pariiskaya, and L. P. Pitaevskii, Sov. Phys. JETP **22**, 449 (1966).
[40] C. Bostedt, J. D. Bozek, P. H. Bucksbaum, R. N. Coffee, J. B. Hastings, Z. Huang, R. W. Lee, S. Schorb, J. N. Corlett, P. Denes *et al.*, J. Phys. B **46**, 164003 (2013).
[41] C. Bostedt (private communication).
[42] E. Skopalová, Y. C. El-Taha, A. Zaïr, M. Hohenberger, E. Springate, J. W. G. Tisch, R. A. Smith, and J. P. Marangos, Phys. Rev. Lett. **104**, 203401 (2010).
[43] D. D. Hickstein, F. Dollar, J. A. Gaffney, M. E. Foord, G. M. Petrov, B. B. Palm, K. E. Keister, J. L. Ellis, C. Ding, S. B. Libby *et al.*, Phys. Rev. Lett. **112**, 115004 (2014).
[44] G. Kulcsar, D. AlMawlawi, F. W. Budnik, P. R. Herman, M. Moskovits, L. Zhao, and R. S. Marjoribanks, Phys. Rev. Lett. **84**, 5149 (2000).
[45] Z. Qian, A. Mordovanakis, J. E. Schoenly, A. Covarrubias, Y. Feng, L. Lilge, and R. S. Marjoribanks, Biomed. Opt. Express **5**, 208 (2014).